Supplementary Information

Exploring the properties of lead-free hybrid double perovskites using a combined computational-experimental approach

Zeyu Deng, Fengxia Wei, Shijing Sun, Gregor Kieslich, Anthony K. Cheetham* and Paul D. Bristowe*

Department of Materials Science and Metallurgy
University of Cambridge
27 Charles Babbage Road
Cambridge CB3 0FS
United Kingdom

Computational Methodology

The DFT calculations were performed using the Vienna *ab initio* Simulation Package (VASP).[1,2] Projected augmented wave (PAW)[3] pseudopotentials were employed with the following electrons treated explicitly: H ($1s^1$), C ($2s^22p^2$), N ($2s^22p^3$), K ($3s^23p^64s^1$), Bi ($5d^{10}6s^26p^3$), Tl ($5d^{10}6s^26p^1$), Cu ($3p^63d^{10}4s^1$), Ag ($4p^64d^{10}5s^1$), Pb ($5d^{10}6s^26p^2$), Cl ($3s^23p^5$), Br ($4s^24p^5$) and I ($5s^25p^5$). The non-local van der Waals density functional (vdW-DF)[4] was used with the exchange-correlation energy calculated as $E_{xc} = E_x^{GGA} + E_c^{LDA} + E_c^{nl}$, where the exchange energy E_x^{GGA} is obtained from the generalized gradient approximation (GGA) using the optB86b functional, the local correlation energy E_c^{LDA} from the local density approximation (LDA) and the non-local correlation energy E_c^{nl} from double space integration. K-points were sampled in the first Brillouin zone using a 4×4×2 Monkhorst-Pack[5] mesh, and for electronic density of states (DOS) calculations, a finer 8×8×3 mesh was used. A 500 eV plane-wave kinetic energy cutoff was employed for all calculations. The effect of relativistic spin-orbit coupling (SOC) was included in the DOS and electronic band structure calculations. The experimentally synthesized double perovskite $(MA)_2KBiCl_6$ was used as a basis for constructing all the structures which were then relaxed until the interatomic forces were less than 0.01 eV/Å while maintaining the same rhombohedral symmetry as $(MA)_2KBiCl_6$.

1 G. Kresse, *J. Non. Cryst. Solids*, 1995, **192-193**, 222–229.
2 G. Kresse and J. Furthmüller, *Comput. Mater. Sci.*, 1996, **6**, 15–50.
3 P. E. Blochl, *Phys Rev B Condens Matter*, 1994, **50**, 17953-17979.
4 J. Klimes, D. R. Bowler and A. Michaelides, *Phys Rev B*, 2011, **83**.
5 H. J. Monkhorst and J. D. Pack, *Phys Rev B*, 1976, **13**, 5188-5192.

Choice of space group for calculations

We chose to perform all our calculations in $R\bar{3}m$ rather than $Fm\bar{3}m$ for three important reasons: (i) The rhombohedral space group is adopted by one of the lower temperature forms of the hybrid double perovskites and was observed experimentally at room temperature in our previous work on $(MA)_2KBiCl_6$ [ref. 19]; furthermore, we know that this phase becomes cubic $Fm\bar{3}m$ on heating above room temperature; (ii) The B^{I}-X-B^{III} angles can be varied in $R\bar{3}m$ whereas they are fixed by symmetry in $Fm\bar{3}m$; for example, B^{I}-X-B^{III} is calculated to be 174° for $(MA)_2TlBiBr_6$ in $R\bar{3}m$ symmetry whereas it must be held at 180° in $Fm\bar{3}m$. This is important because it has been shown in many papers (e.g. Nano Lett. 14.6 (2014): 3608–3616, Nat. Comm. 5 (2014): 5757) that the electronic band gap depends significantly on the B-X-B angles connecting the inorganic octahedra; (iii) The use of $R\bar{3}m$ fixes the orientation of the MA cation whereas it is disordered and very difficult to model in $Fm\bar{3}m$. We note that the new phase $(MA)_2TlBiBr_6$ is cubic with $Fm\bar{3}m$ symmetry at room temperature but that the DSC curve (Figure S15) shows two phase transitions at lower temperatures. It is reasonable to expect that one of the resulting structures has $R\bar{3}m$ symmetry based on our earlier work on $(MA)_2KBiCl_6$ [ref. 19].

Thus the assumption of $R\bar{3}m$ symmetry in the present calculations is well justified and, furthermore, allows trends in behavior to be studied when the chemistry is changed but the symmetry is not. This is supported by the fact that the calculations agree well with our experimental measurements for the trend in band gaps and Young's moduli.

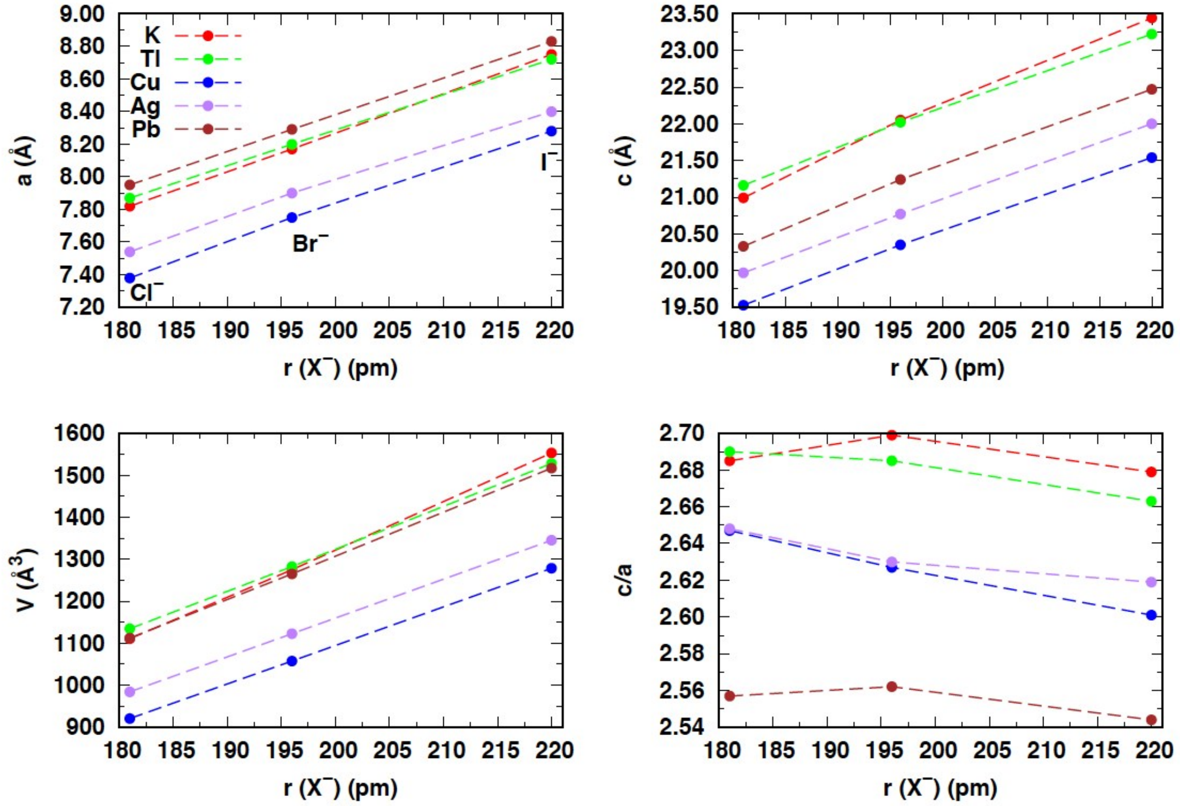

Figure S1 Computed lattice constants, equilibrium volumes and c/a ratios of $(MA)_2B^IB^{III}X_6$ as a function of the radius of anion X.

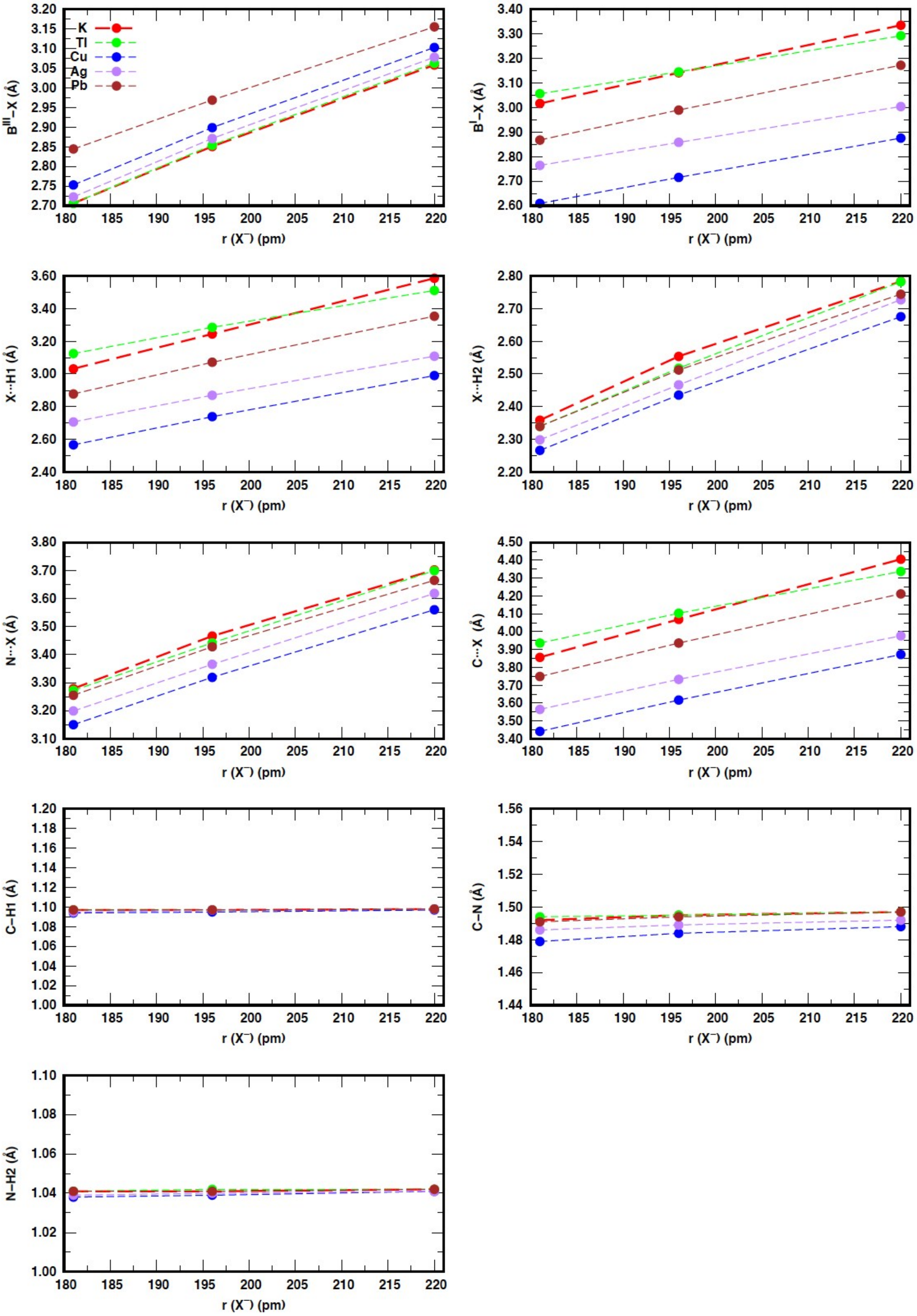

Figure S2 Computed interatomic distances in $(MA)_2B^IB^{III}X_6$ as a function of the radius of anion X.

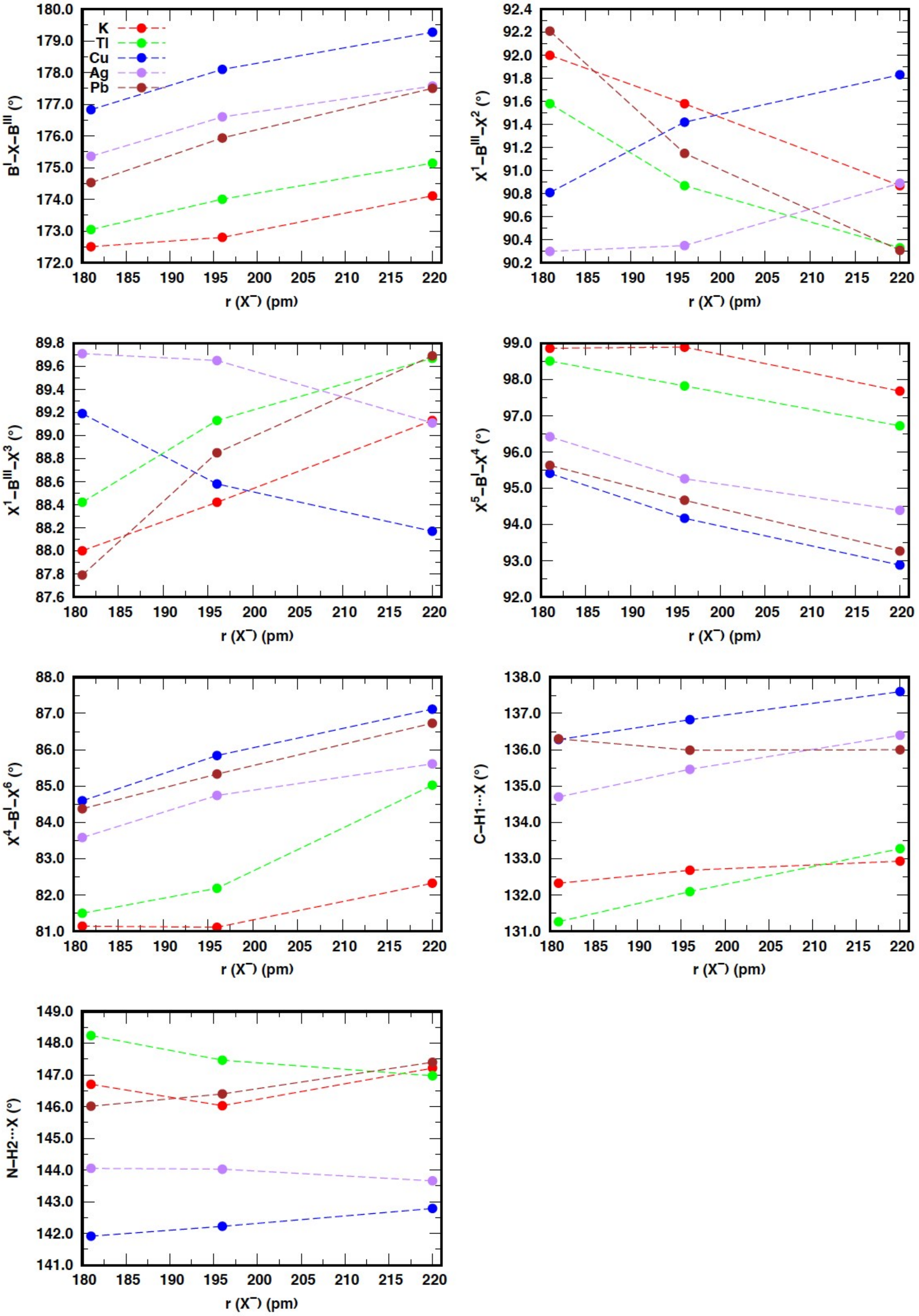

Figure S3 Computed bond angles in $(MA)_2B^IB^{III}X_6$ as a function of the radius of anion X.

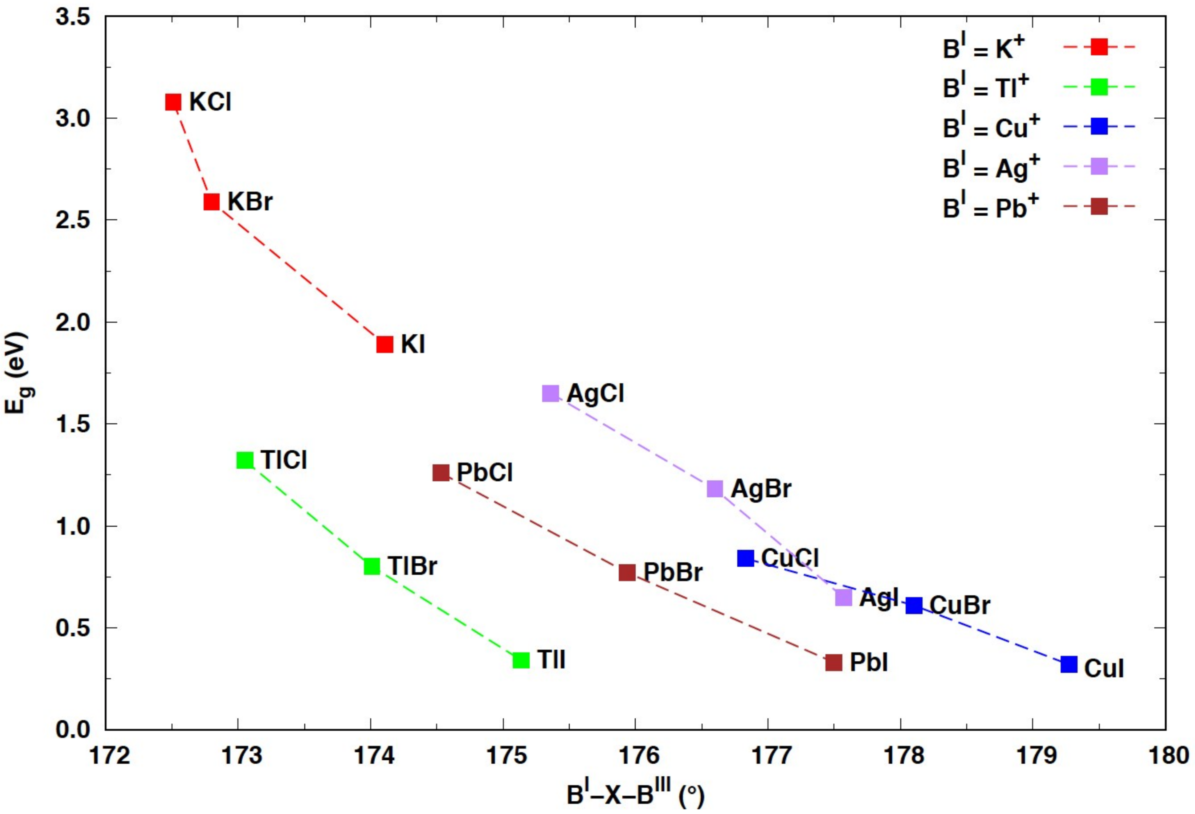

Figure S4 Computed band gaps of $(MA)_2B^IB^{III}X_6$ as a function of the B^I-X-B^{III} bond angle.

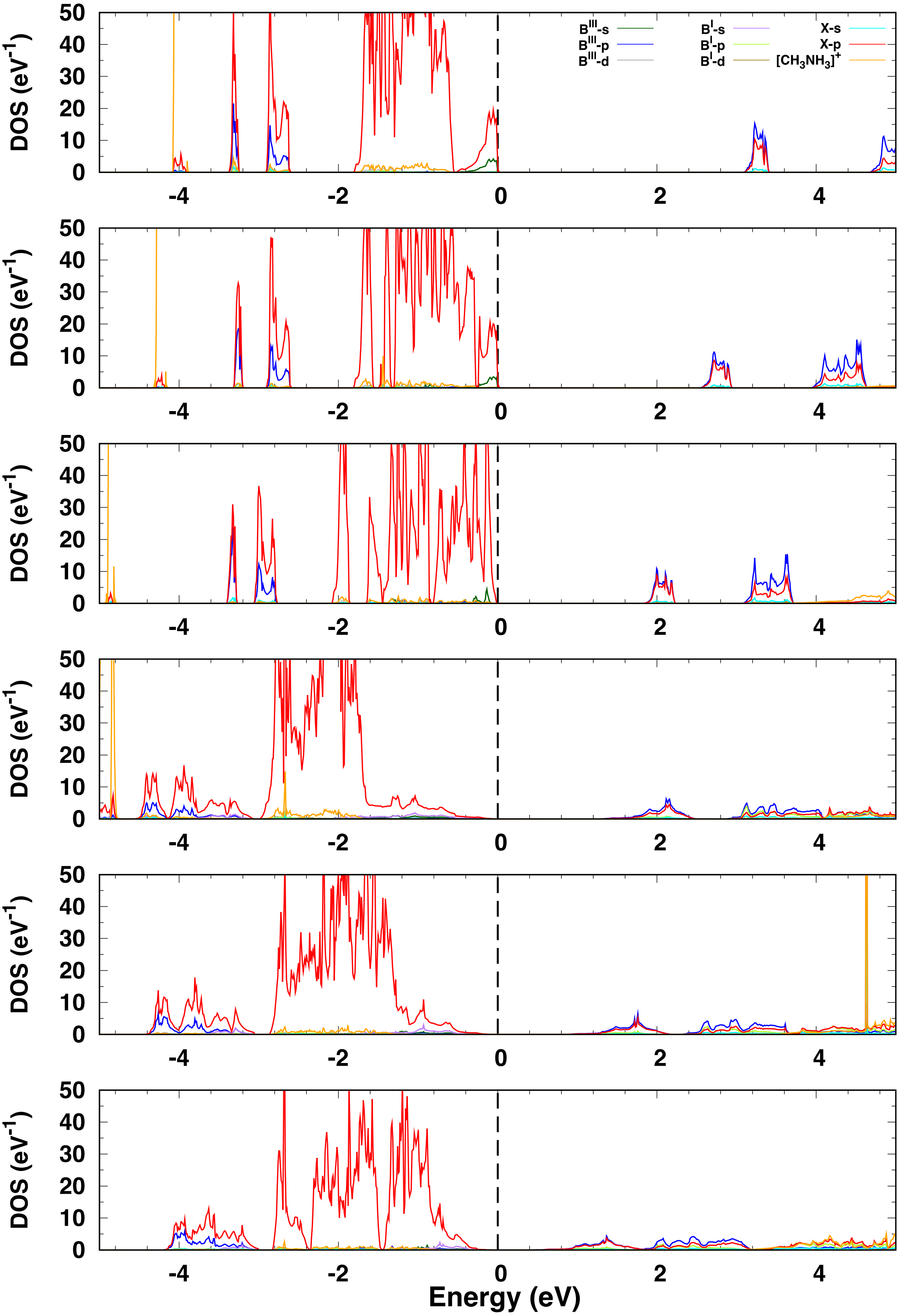

Figure S5 Computed PDOS of $(MA)_2B^IB^{III}X_6$, where B^{III} = Bi, B^I = K and Tl, X = Cl, Br and I. From top to bottom: $(MA)_2KBiCl_6$, $(MA)_2KBiBr_6$, $(MA)_2KBiI_6$, $(MA)_2TlBiCl_6$, $(MA)_2TlBiBr_6$ and $(MA)_2TlBiI_6$.

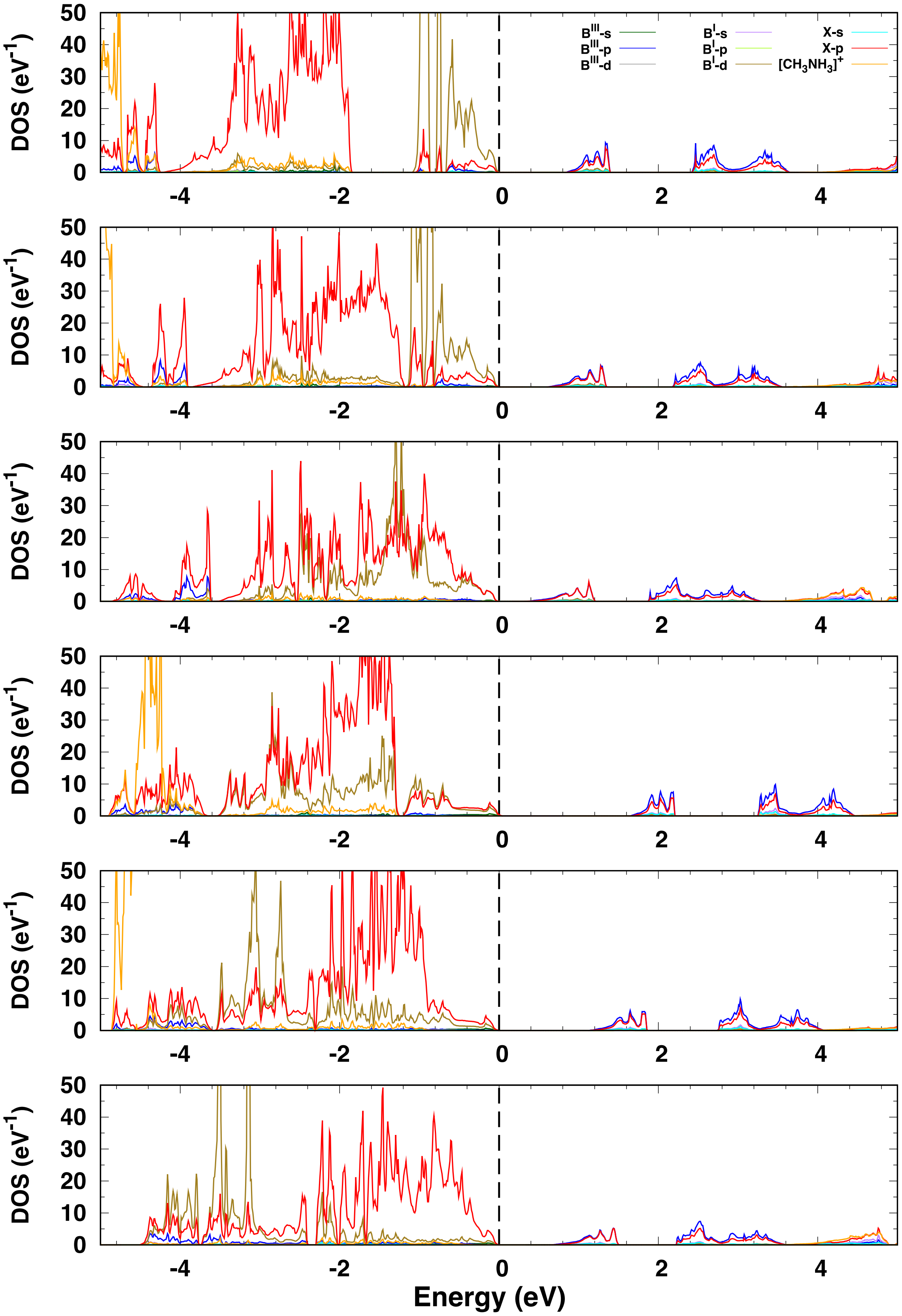

Figure S6 Computed PDOS of $(MA)_2B^IB^{III}X_6$, where B^{III} = Bi, B^I = Cu and Ag, X = Cl, Br and I. From top to bottom: $(MA)_2CuBiCl_6$, $(MA)_2CuBiBr_6$, $(MA)_2CuBiI_6$, $(MA)_2AgBiCl_6$, $(MA)_2AgBiBr_6$ and $(MA)_2AgBiI_6$.

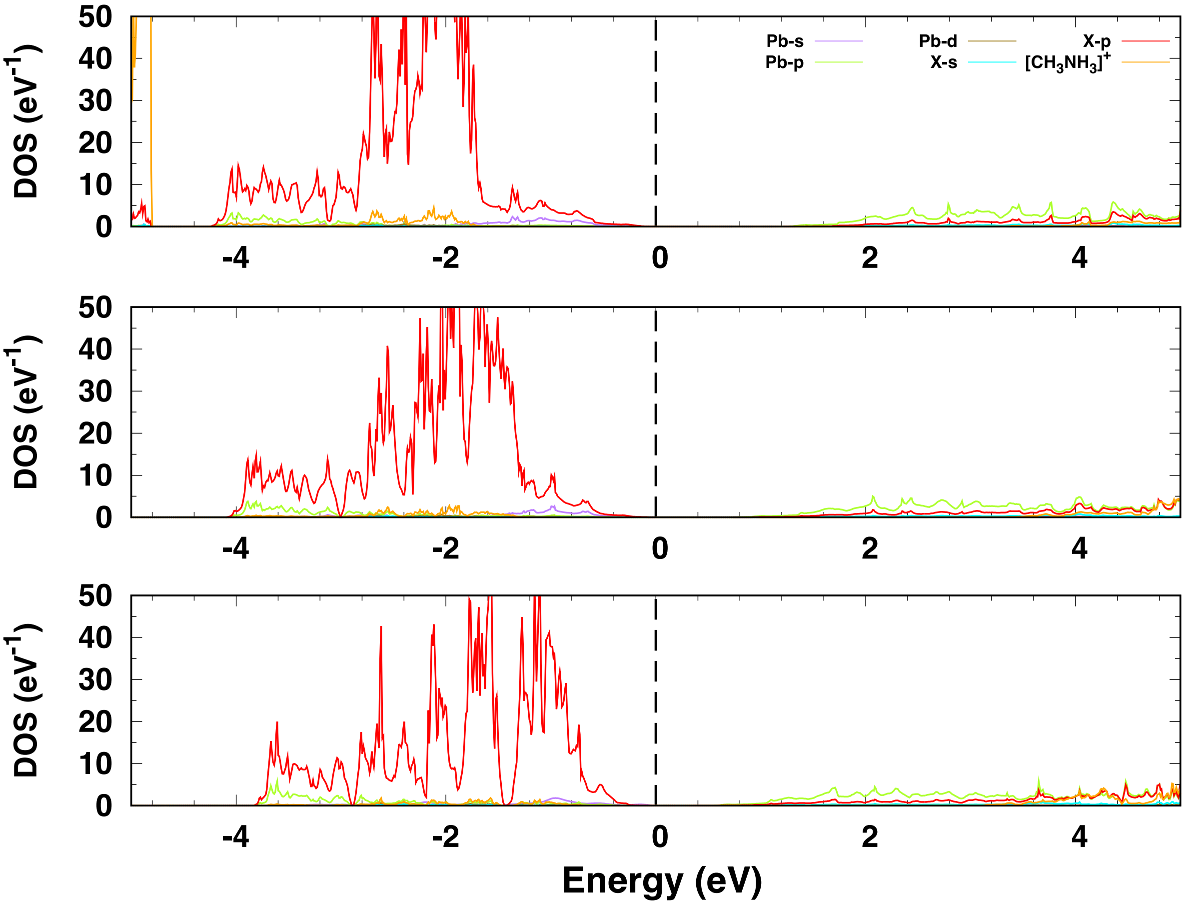

Figure S7 Computed PDOS of $MAPbX_3$. From top to bottom: $MAPbCl_3$, $MAPbBr_3$ and $MAPbI_3$.

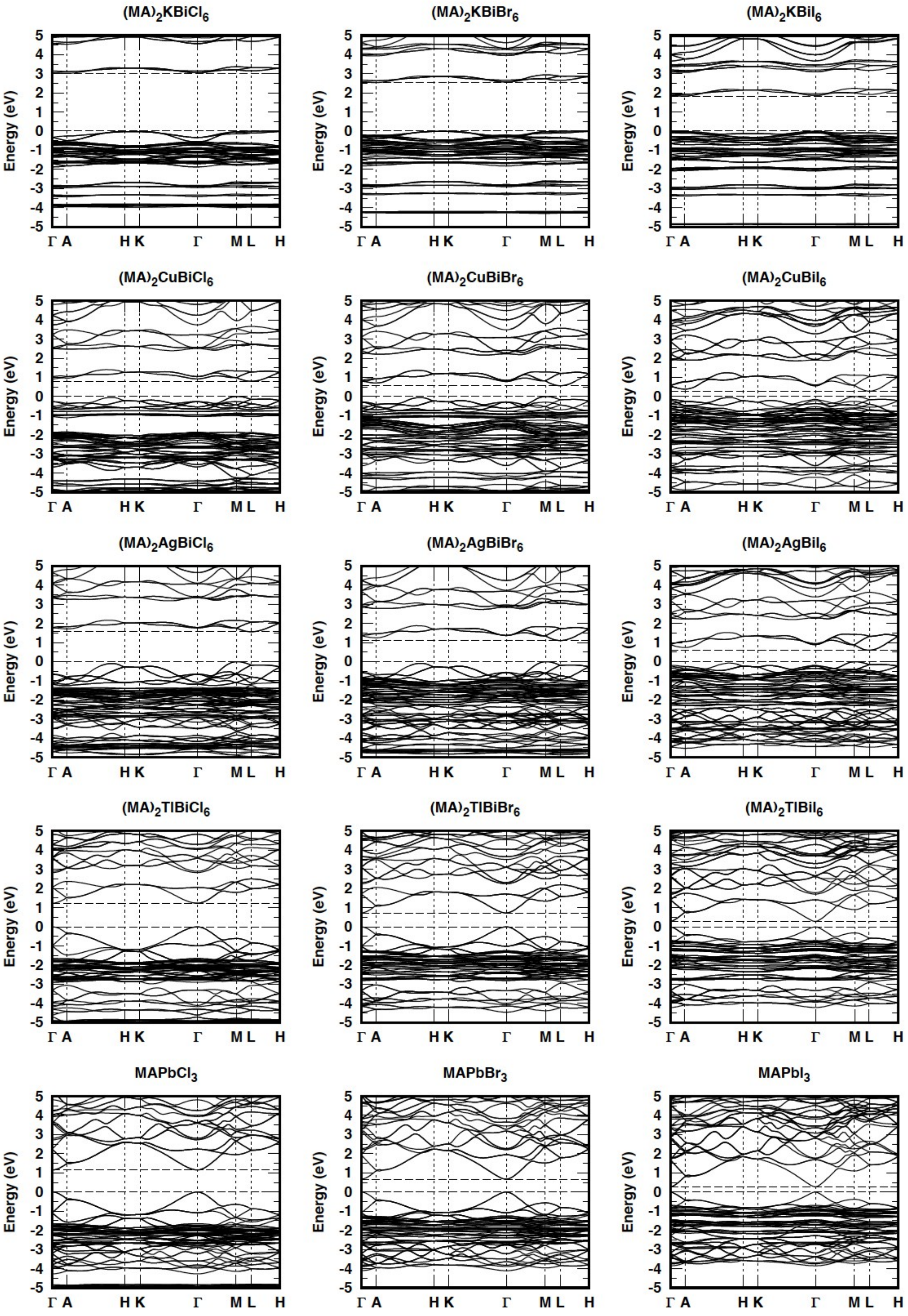

Figure S8 Computed band structures of (MA)$_2$B^{I}B^{III}X$_6$ including MAPbX$_3$. The following high symmetry points in the first Brillouin zone were used: Γ (0,0,0), A (0,0,0.5), H (-0.333,0.667,0.5), K (-0.333,0.667,0), M (0,0.5,0) and L (0,0.5,0.5).

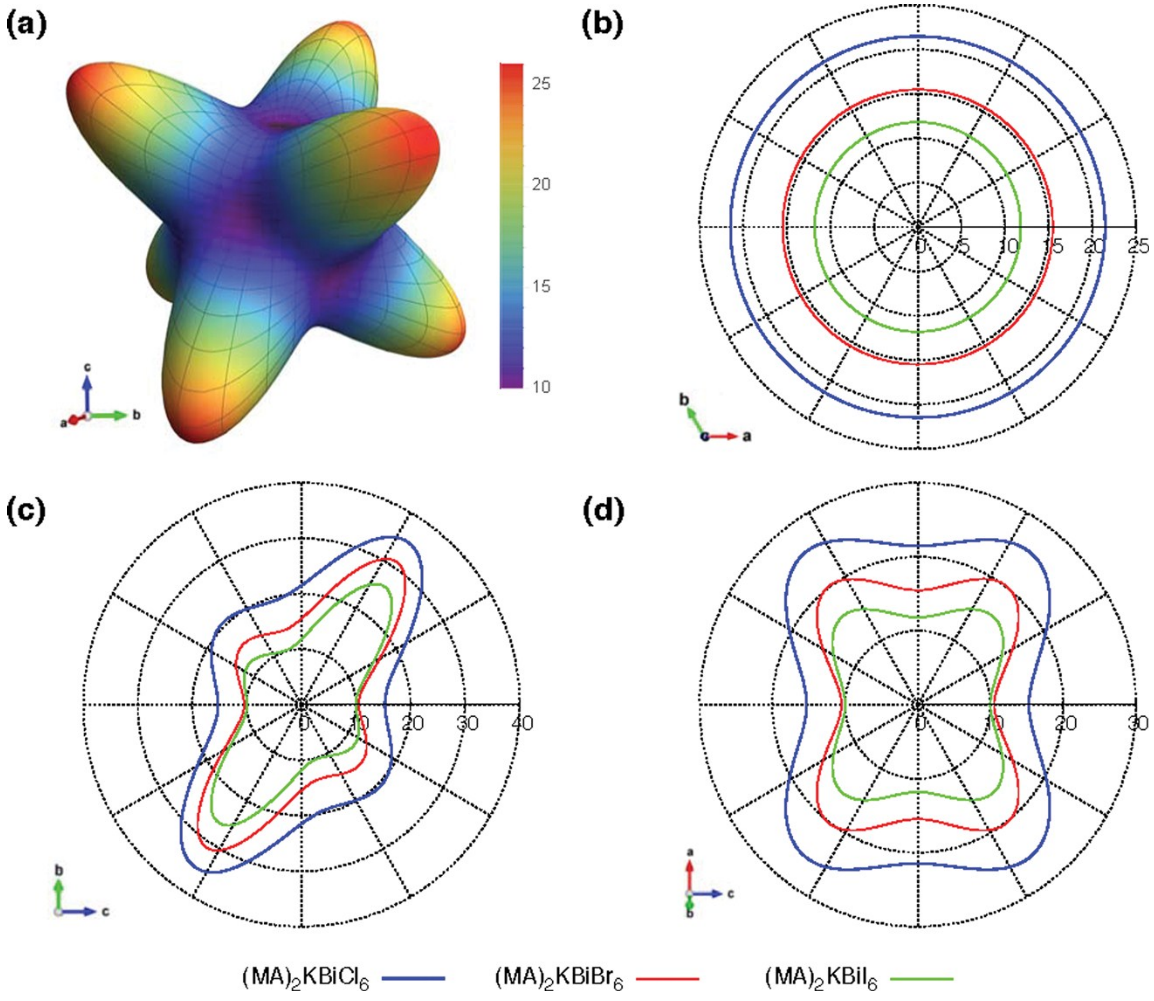

Figure S9 (a) Computed 3D directional Young's modulus of $(MA)_2KBiI_6$ and the corresponding contour plots for $(MA)_2KBiX_6$ on (b) the (001) plane (c) the plane perpendicular to [100] and (d) the (010) plane. The values are referred to hexagonal axes. The c-direction is along [001] in the rhombohedral structure or equivalently [111] in the cubic structure. Units shown are in GPa.

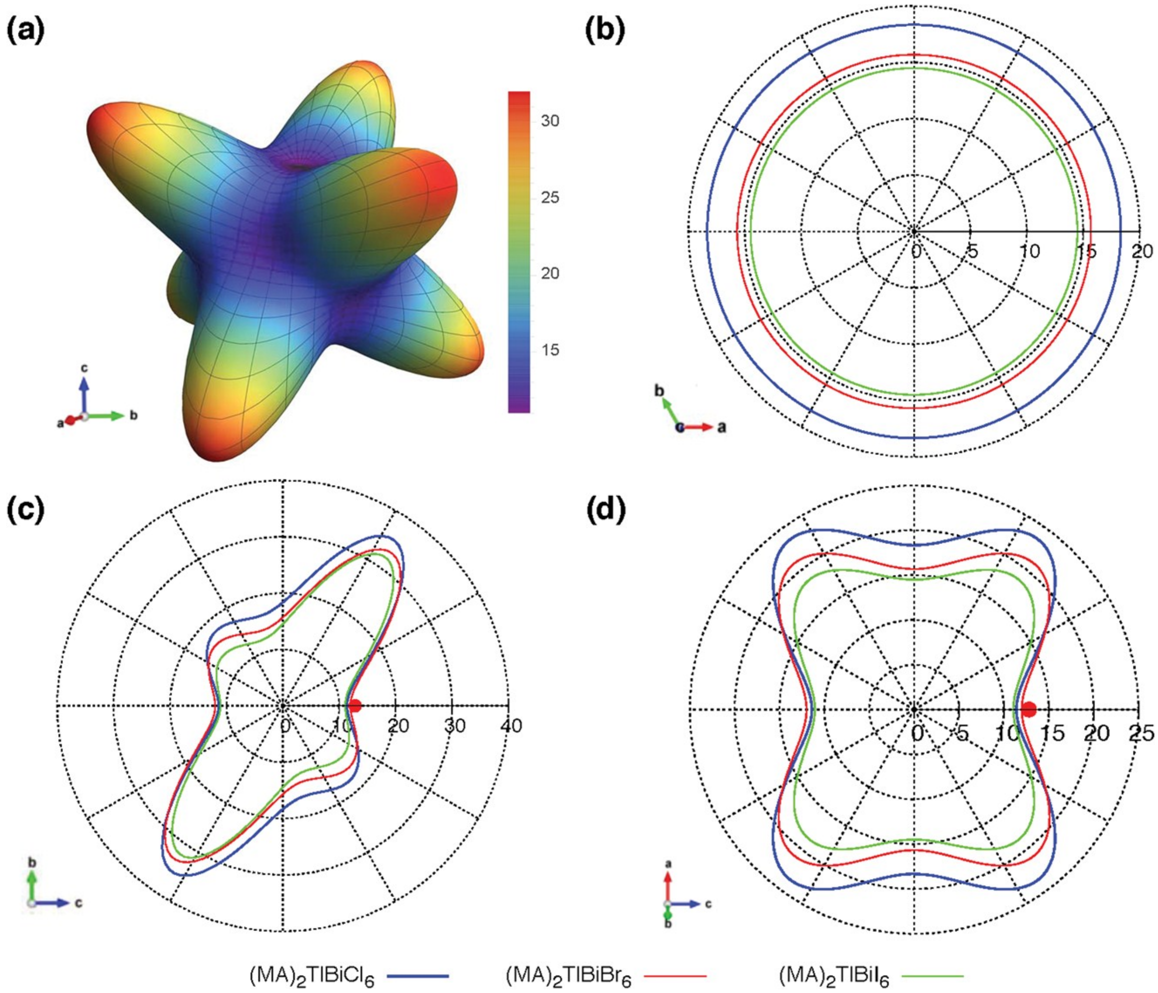

Figure S10 (a) Computed 3D directional Young's modulus of $(MA)_2TlBiI_6$ and the corresponding contour plots for $(MA)_2TlBiX_6$ on (b) the (001) plane (c) the plane perpendicular to [100] and (d) the (010) plane. The values are referred to hexagonal axes. The c-direction is along [001] in the rhombohedral structure or equivalently [111] in the cubic structure. The red dots indicate the experimental measurement for $(MA)_2TlBiBr_6$. Units shown are in GPa.

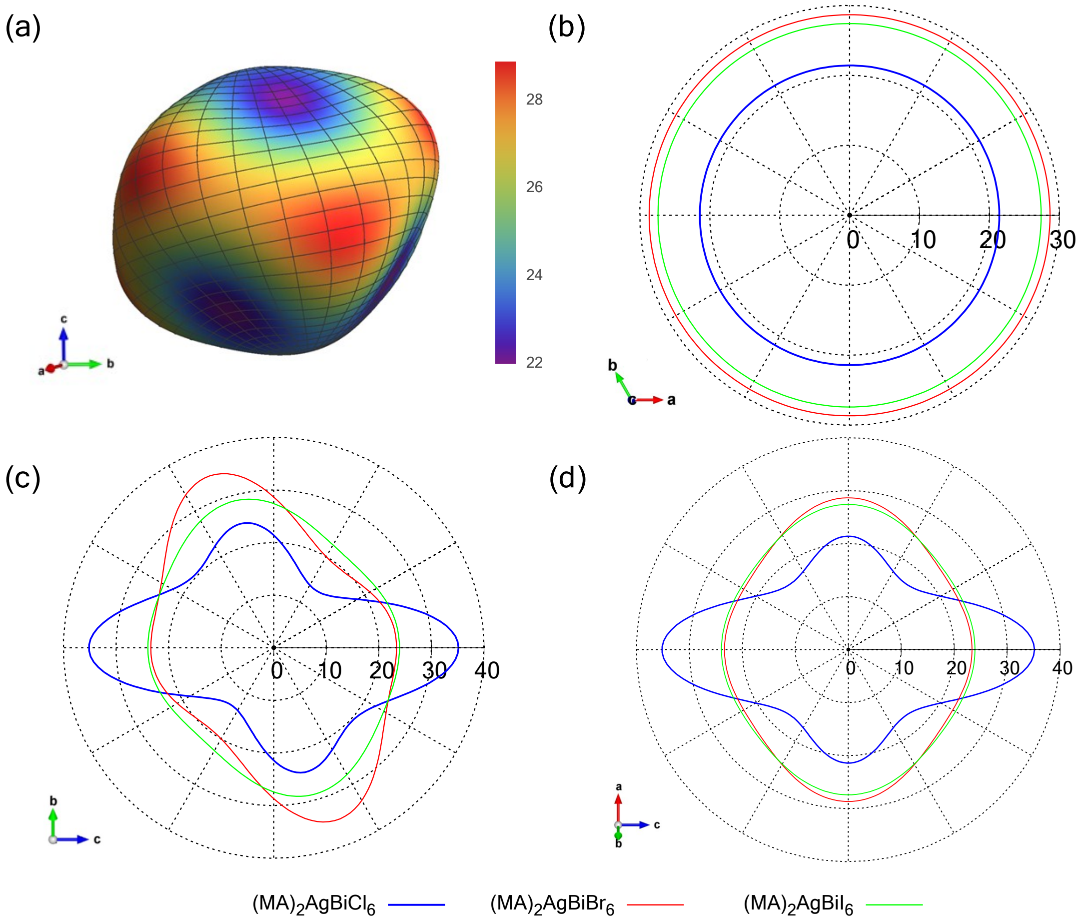

Figure S11 (a) Computed 3D directional Young's modulus of $(MA)_2AgBiI_6$ and the corresponding contour plots for $(MA)_2AgBiX_6$ on (b) the (001) plane (c) the plane perpendicular to [100] and (d) the (010) plane. The values are referred to hexagonal axes. The c-direction is along [001] in the rhombohedral structure or equivalently [111] in the cubic structure. Units shown are in GPa.

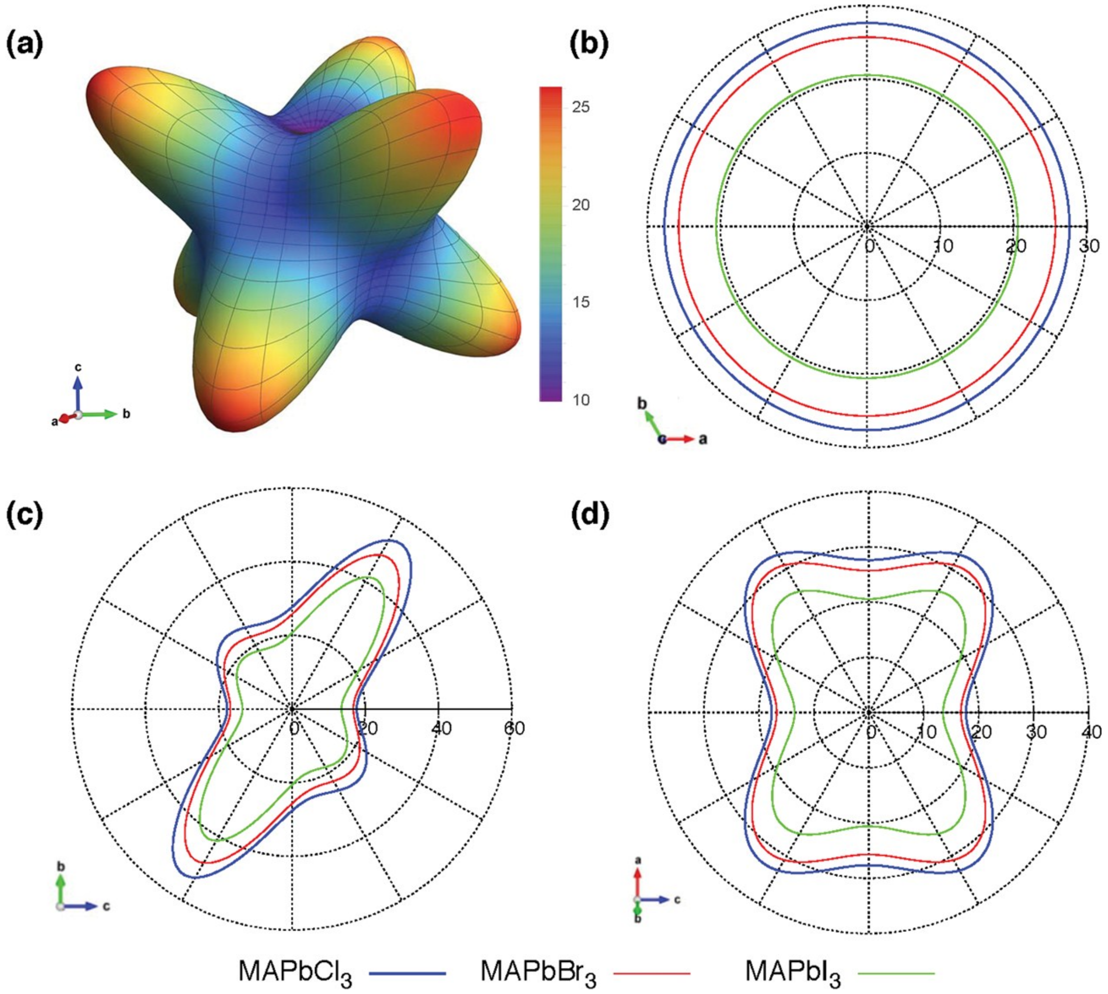

Figure S12 (a) Computed 3D directional Young's modulus of $MAPbI_3$ and the corresponding contour plots for $MAPbX_3$ on (b) the (001) plane (c) the plane perpendicular to [100] and (d) the (010) plane. The values are referred to hexagonal axes. The c-direction is along [001] in the rhombohedral structure or equivalently [111] in the cubic structure. Units shown are in GPa.

Notes on the computed Young's moduli

For $(MA)_2KBiX_6$, $(MA)_2TlBiX_6$ and $MAPbX_3$, the maximum and minimum values lie along B-X bond directions and the diagonal of the B-X cage, respectively. However, for $(MA)_2AgBiX_6$ (and $(MA)_2CuBiI_6$ not shown) these maxima and minima reverse directions. This can be explained in terms of the incompressibility of the MA^+ cation and the Goldschmidt tolerance factors (see Table S8).[6] Previous experimental studies on $MAPbCl_3$ showed that the most rigid component of the structure is the MA^+ cation rather than the $PbCl_6$ octahedra.[7] Also, as Figure S2 shows, when incorporating different X and B^I ions, most bond lengths change by around 0.3 ~ 0.4 Å whereas the change in C-N bond length is much smaller at less than 0.01 Å. The tolerance factor for $(MA)_2AgBiX_6$ is relatively large, implying that the B^IXB^{III} framework is too small for the MA^+ cation. Therefore, because MA^+ is incompressible and the framework is too small, when applying strains, the intramolecular interactions between MA^+ and the framework either make MA^+ rotate, or compress the C-N, C-H or N-H bonds, inducing a large change in stress. The MA^+ rotations result in the nonlinear stress-strain relationship found in the calculations for those structures with large tolerance factors, and the bond compressions make the Young's moduli along the C-N, C-H or N-H directions exhibit a maximum.

[6] Kieslich, G.; Sun, S.; Cheetham, A. K. *Chem. Sci.* **2014**, *5*, 4712–4715.

[7] Chi, L.; Swainson, I.; Cranswick, L.; Her, J.-H.; Stephens, P.; Knop, O. *J. Solid State Chem.* **2005**, *178*, 1376–1385.

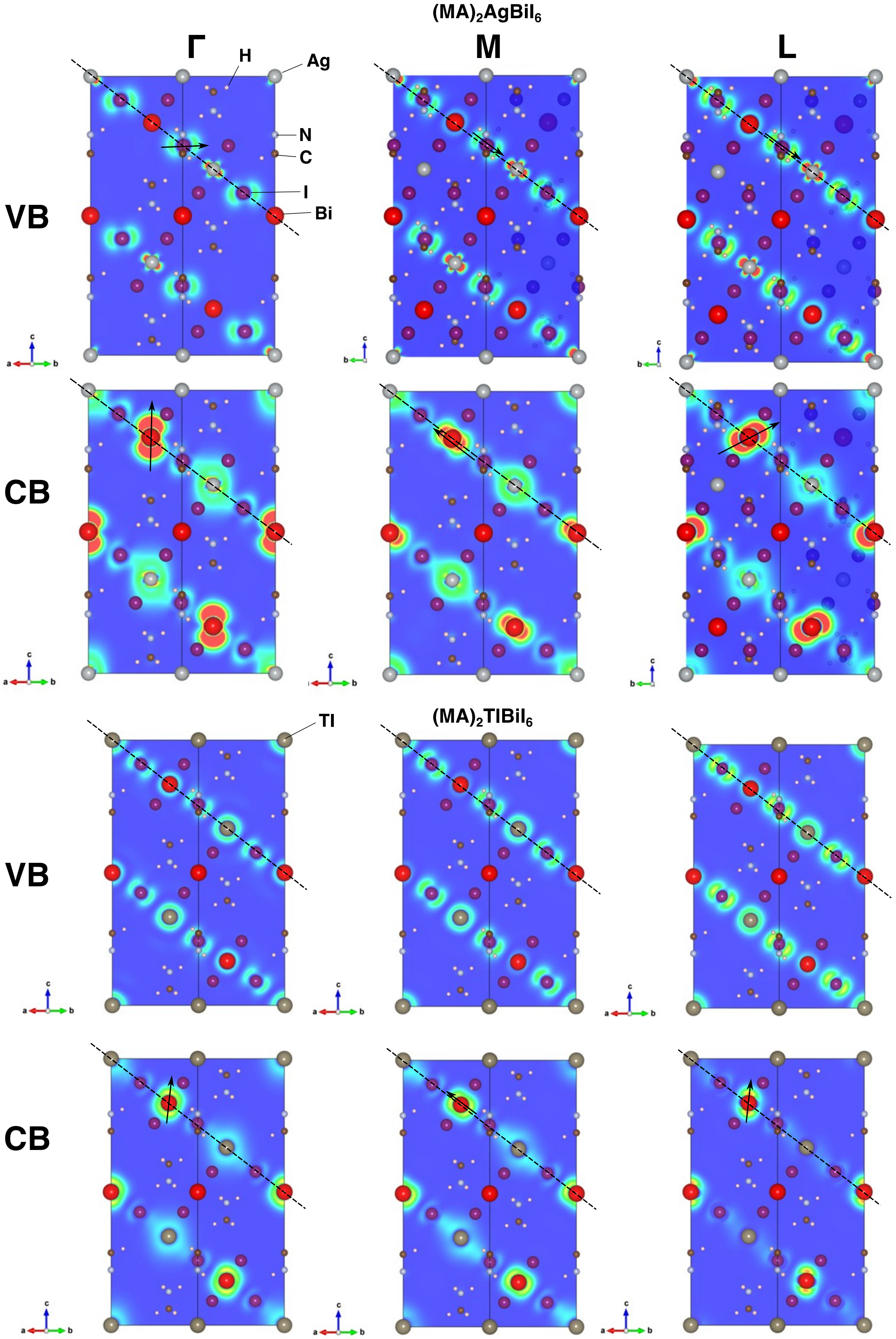

Figure S13 Band decomposed charge densities near the top of the valence band (VB) and the bottom of the conduction band (CB) at Γ, M and L for (MA)$_2$AgBiI$_6$ and (MA)$_2$TlBiI$_6$. See notes below for explanation. Density levels are shown from 0 (blue) to 0.003 (red) in units of e/Å^3.

Notes on Figure S13

In order to understand why $(MA)_2AgBiX_6$ and $(MA)_2CuBiX_6$ exhibit an indirect band gap while other compositions have a direct band gap, we take $(MA)_2AgBiI_6$ and $(MA)_2TlBiI_6$ as examples and analyze their band decomposed charge densities near the band edges. These are shown in Figure S13 where three high symmetry k-points, Γ (VBM and CBM of $(MA)_2TlBiI_6$), M (VBM of $(MA)_2AgBiI_6$) and L (CBM of $(MA)_2AgBiI_6$) are considered. Note that Ag^+ and Tl^+ differ fundamentally in that the latter has two valence electrons in the 6s orbital.

For $(MA)_2AgBiI_6$, the VB edge states consist mostly of Ag-4d and I-5p anti-bonding states whereas the CB edge states have contributions from Ag-5s and I-5p bonding states plus Bi-6p and I-5p anti-bonding states. In the VB, at M and L, the Ag-4d and I-5p states (pictured with black arrows) are aligned in the same direction while at Γ the states are not aligned in the same direction, and this orbital orientation makes the energy of the anti-bonding states at M and L higher than at Γ. In addition, at M there is more electron density than at L for the anti-bonding states (this is seen from the wave function characters not shown here), so the states at M have the highest energy. Therefore the VBM is located at M instead of Γ or L. In the CB, the orientation of the Bi-6p orbitals at M are more parallel to the Ag-I-Bi direction (shown as dashed lines) than Γ or L, making the energy of the anti-bonding states at L the lowest. Hence, the CBM is at L.

For $(MA)_2TlBiI_6$, the VB edge states consist mostly Tl-6s and I-5p anti-bonding states plus the anti-bonding states of Bi-6s and I-5p whereas the CB edge states have contributions from Tl-6s and I-5p bonding states plus the anti-bonding states of Bi-6p and I-5p. In the VB, the contribution from Bi-6s states is higher at Γ than at M or L, leading to a stronger anti-bonding interaction, which results in the highest energy anti-bonding state at Γ. In the CB, the contributions from Tl-6s,6p and I-5p states at Γ are higher than at M and L, and the orientation of the Bi-6p orbital at Γ is more perpendicular to the Tl-I-Bi direction (shown as dashed lines) than the corresponding orbitals at M. Also at Γ there is a stronger contribution from Tl-6s,6p and I-5p bonding states than at L. Thus, altogether, the energy at Γ is much lower than at M or L in the CB. Hence both the CBM and the VBM are located at Γ.

In summary, specific orbital interactions introduced by the different elements result in energy shifts at different k-points in the band structures, making $(MA)_2AgBiX_6$ and $(MA)_2CuBiX_6$ indirect band gap materials while others are direct band gap materials.

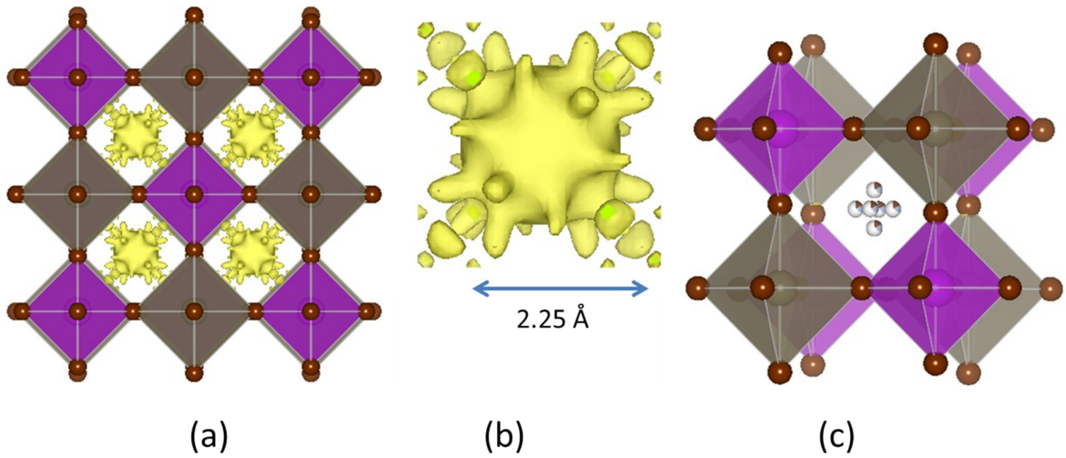

Figure S14 (a) Crystal structure of $(MA)_2TlBiBr_6$ obtained from single crystal X-ray diffraction. $TlBr_6$ and $BiBr_6$ octahedra are grey and purple respectively. MA^+ cation is shown as the electron density (b) the shape of the electron density and (c) MA^+ cation is modeled as the octahedron inside the cavity with restrained C-N bond length 1.4 Å.

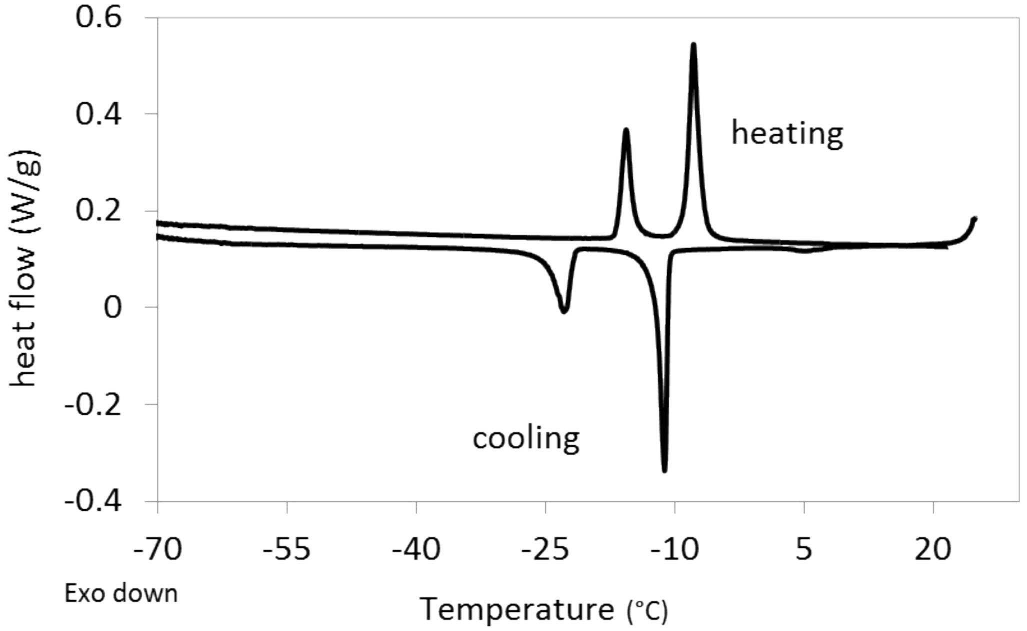

Figure S15 DSC curve of $(MA)_2TlBiBr_6$.

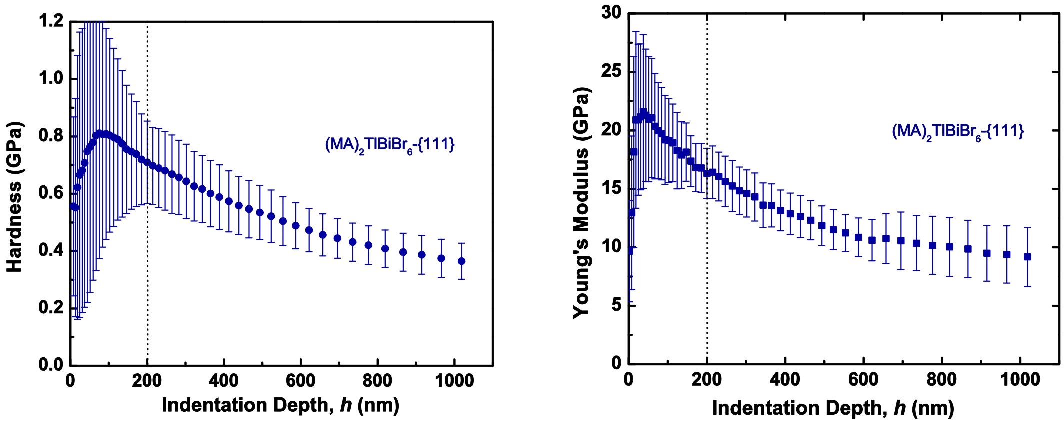

Figure S16 Experimental hardness and Young's Modulus for $(MA)_2TlBiBr_6$ from nanoindentation, averaging from 200 nm to 980 nm of 6 indents

Table S1 Computed lattice constants (Å), equilibrium volumes (Å^3) and c/a ratios of $(MA)_2B^IB^{III}X_6$

A	B^I	B^{III}	X	a	c	V	c/a
MA	K	Bi	Cl	7.82	20.99	1110.64	2.69
MA	K	Bi	Br	8.17	22.05	1274.99	2.70
MA	K	Bi	I	8.75	23.44	1553.34	2.68
MA	Tl	Bi	Cl	7.87	21.16	1134.52	2.69
MA	Tl	Bi	Br	8.20	22.02	1282.42	2.69
MA	Tl	Bi	I	8.72	23.22	1528.19	2.66
MA	Cu	Bi	Cl	7.38	19.53	920.57	2.65
MA	Cu	Bi	Br	7.75	20.35	1057.67	2.63
MA	Cu	Bi	I	8.28	21.54	1278.68	2.60
MA	Ag	Bi	Cl	7.54	19.97	984.27	2.65
MA	Ag	Bi	Br	7.90	20.77	1122.54	2.63
MA	Ag	Bi	I	8.40	22.00	1345.23	2.62
MA	Pb	Pb	Cl	7.95	20.33	1112.42	2.56
MA	Pb	Pb	Br	8.29	21.24	1265.21	2.56
MA	Pb	Pb	I	8.83	22.47	1517.20	2.54

Table S2 Computed interatomic distances (Å) of $(MA)_2B^{I}B^{III}X_6$

A	B^{I}	B^{III}	X	B^{III}-X	B^{I}-X	X···H1	X···H2	N···X	C···X	C-N	C-H1	N-H2
MA	K	Bi	Cl	2.706	3.016	3.032	2.359	3.279	3.856	1.492	1.097	1.041
MA	K	Bi	Br	2.851	3.141	3.245	2.554	3.466	4.069	1.495	1.097	1.041
MA	K	Bi	I	3.058	3.335	3.585	2.783	3.702	4.406	1.497	1.098	1.042
MA	Tl	Bi	Cl	2.706	3.056	3.125	2.340	3.272	3.936	1.494	1.097	1.041
MA	Tl	Bi	Br	2.854	3.145	3.286	2.518	3.442	4.103	1.495	1.097	1.042
MA	Tl	Bi	I	3.063	3.292	3.511	2.782	3.699	4.337	1.497	1.098	1.042
MA	Cu	Bi	Cl	2.753	2.609	2.567	2.267	3.150	3.441	1.479	1.094	1.038
MA	Cu	Bi	Br	2.899	2.715	2.739	2.436	3.319	3.617	1.484	1.095	1.039
MA	Cu	Bi	I	3.103	2.875	2.990	2.675	3.560	3.872	1.488	1.097	1.041
MA	Ag	Bi	Cl	2.722	2.764	2.708	2.299	3.199	3.565	1.486	1.095	1.039
MA	Ag	Bi	Br	2.871	2.858	2.871	2.467	3.365	3.733	1.489	1.097	1.040
MA	Ag	Bi	I	3.078	3.004	3.109	2.727	3.618	3.976	1.492	1.098	1.041
MA	Pb	Pb	Cl	2.844	2.868	2.878	2.340	3.255	3.748	1.491	1.097	1.041
MA	Pb	Pb	Br	2.969	2.990	3.072	2.512	3.428	3.936	1.494	1.097	1.041
MA	Pb	Pb	I	3.155	3.172	3.353	2.744	3.665	4.212	1.497	1.098	1.042

Table S3 Computed bond angles (°) in $(MA)_2B^IB^{III}X_6$.

A	B^I	B^{III}	X	B^I-X-B^{III}	X^1-B^{III}-X^2	X^1-B^{III}-X^2	X^5-B^I-X^4	X^4-B^I-X^6	C-H1···X	N-H2···X
MA	K	Bi	Cl	172.51	92.00	88.00	98.86	81.14	132.32	146.70
MA	K	Bi	Br	172.80	91.58	88.42	98.89	81.11	132.68	146.03
MA	K	Bi	I	174.11	90.87	89.13	97.68	82.32	132.93	147.21
MA	Tl	Bi	Cl	173.05	91.58	88.42	98.51	81.49	131.26	148.24
MA	Tl	Bi	Br	174.01	90.87	89.13	97.82	82.18	132.09	147.46
MA	Tl	Bi	I	175.14	90.33	89.67	96.72	85.02	133.27	146.97
MA	Cu	Bi	Cl	176.83	90.81	89.19	95.41	84.59	136.28	141.92
MA	Cu	Bi	Br	178.10	91.42	88.58	94.17	85.84	136.83	142.23
MA	Cu	Bi	I	179.27	91.83	88.17	92.88	87.12	137.60	142.79
MA	Ag	Bi	Cl	175.36	90.30	89.71	96.42	83.58	134.70	144.05
MA	Ag	Bi	Br	176.60	90.35	89.65	95.26	84.74	135.46	144.03
MA	Ag	Bi	I	177.57	90.89	89.11	94.39	85.61	136.40	143.66
MA	Pb	Pb	Cl	174.53	92.21	87.79	95.63	84.37	136.30	146.01
MA	Pb	Pb	Br	175.94	91.15	88.85	94.67	85.33	135.99	146.40
MA	Pb	Pb	I	177.50	90.31	89.69	93.27	86.73	136.00	147.40

Table S4 Computed band gaps (eV) of $(MA)_2B^IB^{III}X_6$ with experimental values for $(MA)_2KBiCl_6$ and $(MA)_2TlBiBr_6$.

A	B^I	B^{III}	X	E_g (DFT+SOC)	E_g (exp)
MA	K	Bi	Cl	3.02	3.04
MA	K	Bi	Br	2.54	
MA	K	Bi	I	1.84	
MA	Tl	Bi	Cl	1.23	
MA	Tl	Bi	Br	0.72	2.16
MA	Tl	Bi	I	0.28	
MA	Cu	Bi	Cl	0.79	
MA	Cu	Bi	Br	0.56	
MA	Cu	Bi	I	0.28	
MA	Ag	Bi	Cl	1.57	
MA	Ag	Bi	Br	1.11	
MA	Ag	Bi	I	0.60	
MA	Pb	Pb	Cl	1.15	
MA	Pb	Pb	Br	0.67	
MA	Pb	Pb	I	0.27	

Table S5 Computed positions of the valence band maximum (VBM) and conduction band minimum (CBM) for $(MA)_2B^IB^{III}X_6$

A	B^I	B^{III}	X	VBM	CBM
MA	K	Bi	Cl	L	A
MA	K	Bi	Br	Near L	A
MA	K	Bi	I	Γ	A
MA	Tl	Bi	Cl	Γ	Γ
MA	Tl	Bi	Br	Γ	Γ
MA	Tl	Bi	I	Γ	Γ
MA	Cu	Bi	Cl	M	L
MA	Cu	Bi	Br	M	L
MA	Cu	Bi	I	M	L
MA	Ag	Bi	Cl	M	L
MA	Ag	Bi	Br	M	L
MA	Ag	Bi	I	M	L
MA	Pb	Pb	Cl	Γ	Γ
MA	Pb	Pb	Br	Γ	Γ
MA	Pb	Pb	I	Γ	Γ

Table S6 Computed single crystal elastic stiffness constants (C_{ij}) of $(MA)_2B^IB^{III}X_6$. All units are in GPa

A	B^I	B^{III}	X	C_{11}	C_{12}	C_{13}	C_{14}	C_{33}	C_{44}	C_{66}
MA	K	Bi	Cl	31.75	11.75	14.38	-3.58	24.79	12.11	10.00
MA	K	Bi	Br	25.03	9.13	11.99	-3.89	18.90	10.68	7.95
MA	K	Bi	I	19.60	7.15	9.97	-3.58	17.40	8.94	6.23
MA	Tl	Bi	Cl	29.79	10.73	14.28	-4.29	21.45	11.86	9.53
MA	Tl	Bi	Br	25.91	9.43	13.36	-4.28	22.08	11.35	8.24
MA	Tl	Bi	I	24.29	8.52	11.72	-4.59	19.42	10.69	7.89
MA	Cu	Bi	Cl	55.40	33.67	21.95	13.81	57.62	5.70	10.86
MA	Cu	Bi	Br	50.49	26.65	20.75	7.96	43.25	4.79	11.92
MA	Cu	Bi	I	44.75	20.24	15.96	5.19	38.27	6.15	12.26
MA	Ag	Bi	Cl	47.23	28.00	24.07	3.44	36.46	10.30	9.61
MA	Ag	Bi	Br	43.93	20.64	18.87	3.04	34.39	9.19	11.65
MA	Ag	Bi	I	38.21	16.99	16.02	1.19	33.22	8.84	10.61
MA	Pb	Pb	Cl	45.67	17.40	22.15	-6.56	33.22	17.91	14.14
MA	Pb	Pb	Br	40.67	13.86	18.48	-6.30	29.26	15.93	13.41
MA	Pb	Pb	I	33.15	10.92	15.08	-5.76	23.82	13.96	11.12

Table S7 Computed polycrystalline elastic Young's modulus (E), bulk modulus (B), shear modulus (G), Poisson's ratio (ν) as well as the range of corresponding single crystal elastic moduli of $(MA)_2B^IB^{III}X_6$. All units are in GPa except Poisson's ratio. $(MA)_2CuBiCl_6$ and $(MA)_2CuBiBr_6$ are not mechanically stable therefore values are not shown.

A	B^I	B^{III}	X	E	B	G	ν	E_{max}	E_{min}	G_{max}	G_{min}	$ν_{max}$	$ν_{min}$
MA	K	Bi	Cl	24.03	18.75	9.34	0.29	35.17	15.29	14.78	6.28	0.50	0.10
MA	K	Bi	Br	18.85	14.97	7.31	0.29	31.06	10.49	13.44	4.28	0.58	0.05
MA	K	Bi	I	15.33	12.31	5.93	0.29	26.14	9.97	11.41	3.66	0.62	0.06
MA	Tl	Bi	Cl	21.70	17.64	8.38	0.29	35.38	11.38	15.13	4.78	0.56	0.07
MA	Tl	Bi	Br	19.90	16.24	7.68	0.30	33.26	11.98	14.35	4.59	0.60	0.07
MA	Tl	Bi	I	18.42	14.64	7.14	0.29	32.01	11.05	14.09	4.24	0.60	0.06
MA	Cu	Bi	Cl	-	-	-	-	-	-	-	-	-	-
MA	Cu	Bi	Br	-	-	-	-	-	-	-	-	-	-
MA	Cu	Bi	I	21.64	25.62	7.96	0.36	30.43	9.20	15.22	3.18	0.96	0.25
MA	Ag	Bi	Cl	25.08	31.00	9.19	0.37	35.45	21.06	13.41	6.50	0.51	0.19
MA	Ag	Bi	Br	26.23	26.31	9.83	0.33	23.36	19.56	13.70	7.14	0.48	0.29
MA	Ag	Bi	I	25.29	23.01	9.60	0.32	23.92	21.99	11.21	8.24	0.39	0.29
MA	Pb	Pb	Cl	32.26	27.39	12.37	0.30	52.53	17.66	22.63	7.28	0.56	0.07
MA	Pb	Pb	Br	29.87	23.45	11.60	0.29	48.74	16.74	21.09	6.94	0.55	0.08
MA	Pb	Pb	I	24.82	19.05	9.68	0.28	41.96	13.50	18.48	5.56	0.57	0.06

Table S8 Computed tolerance factors of $(MA)_2B^IBiX_6$

	Cl	Br	I
K	0.933	0.923	0.907
Cu	1.038	1.021	0.997
Tl	0.915	0.905	0.892
Ag	0.970	0.957	0.939
Pb	0.938	0.927	0.912

Table S9 Fractional coordinates of $(MA)_2TlBiBr_6$ obtained from single crystal XRD

	x	y	z	U_{iso}
Bi	0.5	0.5	0.5	0.0408(9)
Tl	0.5	0.5	0	0.0600(11)
Br	0.5	0.5	0.2625(3)	0.130(2)
C/N	0.19	0.25	0.25	0.050

Table S10 Crystal refinement details for the disordered structure model.

Empirical formula	$C_2N_2Br_6TlBi$
Formula weight	950.9
Temperature/K	298.3(3)
Crystal system	cubic
Space group	$Fm\bar{3}m$
a/Å	11.7616(5)
b/Å	11.7616(5)
c/Å	11.7616(5)
α/°	90
β/°	90
γ/°	90
Volume/Å^3	1627.0(2)
Z	4
μ/mm^{-1}	35.393
F(000)	1600
Crystal size/mm^3	0.1 × 0.1 × 0.1
Radiation	MoKα (λ = 0.71073)
2θ range for data collection/°	6 to 56.198
Index ranges	$-14 \le h \le 12$, $-13 \le k \le 14$, $-15 \le l \le 14$
Reflections collected	1024
Independent reflections	132 [$R_{int} = 0.0649$, $R_{sigma} = 0.0303$]
Data/restraints/parameters	132/0/7
Goodness-of-fit on F^2	1.095
Final R indexes [I>=2σ (I)]	$R_1 = 0.0424$, $wR_2 = 0.1059$
Final R indexes [all data]	$R_1 = 0.0546$, $wR_2 = 0.1169$
Largest diff. peak/hole / e Å^{-3}	1.73/-1.71

Experimental details

The starting material MABr was prepared by mixing stoichiometric amount of methylamine solution (40wt% in H_2O) and HCl (37% in H_2O) at 0°C, heated at 60°C to dryness, then washing with acetone and drying overnight in vacuum oven.

Crystal structure determination was carried out using an Oxford Gemini E Ultra diffractometer, Mo Kα radiation ($\lambda = 0.71073$Å), equipped with an Eos CCD detector. Data collection and reduction were conducted using CrysAliPro (Agilent Technologies). An empirical absorption correction was applied with the Olex2 platform,[8] and the structure was solved using ShelXT[9] and refined by ShelXL.[10]

8 O. V. Dolomano, L. J. Bourhis, R. J. Gildea, J.A.K. Howard and H. Puschmann, *J. Appl. Cryst*, 2009, **42**, 339-341.

9 G. M. Sheldrick, *Acta Cryst. A*, 2015, **71**, 3-8.

10 G. M. Sheldrick, *Acta Cryst. A*, 2008, **64**, 112-122.